Q. J. R. Meteorol. Soc. (1987), **113**, pp. 19–36 551.558.1:551.551.8:551.576.11:551.510.522

Observations of intermittent cumulus convection in the boundary layer

By BURGHARD BRÜMMER and MELCHIOR WENDEL

Meteorologisches Institut, Universität Hamburg
Max-Planck-Institut für Meteorologie, Hamburg

(Received 19 April 1983; revised 30 May 1986. Communicated by Professor H. Charnock)

SUMMARY

During the 1978 JASIN experiment radiosonde and tethered balloon measurements were performed from the *R.V. Meteor*. On 1 September, two cloud layers (cumulus below stratocumulus) were observed below an inversion at about 900 m. Such a boundary layer situation occurred relatively often during the experiment. Cumulus clouds were not present all the time but alternately appeared and disappeared. When they occurred on 1 September, a relatively large vertical shear (about $0{\cdot}006\,s^{-1}$) together with an inflection point in the profile of the wind component normal to the mean wind direction was observed in the cumulus cloud layer. The air–sea temperature difference was small ($\Delta T = -0{\cdot}5$ K) and there was a relatively large dynamical contribution to cloud generation. This may suggest the idea of an interaction between large-scale processes generating a favourable mean wind shear profile and dynamically forced convection.

Significant vertical transport of heat and momentum in the cloud layer occurred only in connection with cumulus clouds. Although in parts of some clouds the transports were locally as large as several $100\,W\,m^{-2}$ and $1\,N\,m^{-2}$, there were only a few events with such large excursions so that the transports averaged over the whole field of cumulus clouds were small.

The relative air flow in and around active cumulus clouds was characterized by updraughts within the cloud and downdraughts at the cloud edges. The thermodynamic properties of updraughts and downdraughts are discussed.

1. INTRODUCTION

The atmospheric boundary layer is often characterized by a particular vertical structure. Underneath a capping temperature inversion there is either a dry mixed layer or—if the surface fluxes and moisture conditions are favourable—a dry mixed layer and an overlying cloud layer with stratocumulus or cumulus clouds. Many observations of such boundary layers have been reported, for example by Warner and Telford (1967), Lenschow (1970), Augstein *et al.* (1974), Pennell and LeMone (1974), Nicholls and LeMone (1980) and Thompson *et al.* (1980) as well as many model simulations, for example by Ball (1960), Lilly (1968), Tennekes (1973), Deardorff (1974), Sommeria (1976), Albrecht *et al.* (1979) and Augstein and Wendel (1980). In this paper observations within a slightly different boundary layer will be described.

In the summer of 1978 the international experiment JASIN (Joint Air Sea Interaction) took place over the NE Atlantic between Scotland and Iceland (Pollard *et al.* 1983). The weather was characterized by small air–sea temperature differences. For water temperatures between 12·0 °C and 13·8 °C the air was never more than 1·5 K warmer or 3·0 K cooler than the water. The extreme differences appeared with southerly or northerly winds. However, due to the prevailing westerly winds the air–sea temperature difference was between +0·3 K and −0·7 K for about 60% of the time. During most of these cases a thin stratocumulus layer was observed below the inversion. Underneath that cloud layer often cumulus clouds developed in isolated form or in the form of cloud fields (Taylor *et al.* 1983). These lower clouds did not occur all the time but alternately appeared and disappeared.

Such a boundary layer structure was observed on 1 September 1978 at the research vessel *Meteor* at 59°N 12·5°W (Fig. 1). An analysis of this situation is presented in this paper using data from radiosondes and a tethered balloon system. Based on the thermodynamic and kinematic structure of the boundary layer before, during and after the passage of a field of low-level cumulus clouds underneath the stratocumulus layer possible reasons for the transient occurrence of the lower clouds are investigated. The

averaged vertical transports of heat and momentum inside and outside the cumulus cloud field are compared and the spatial distribution of the transports within the cloud field and the transports by individual clouds are discussed. Finally, we investigate the relative air flow and the thermodynamic properties in and around individual clouds.

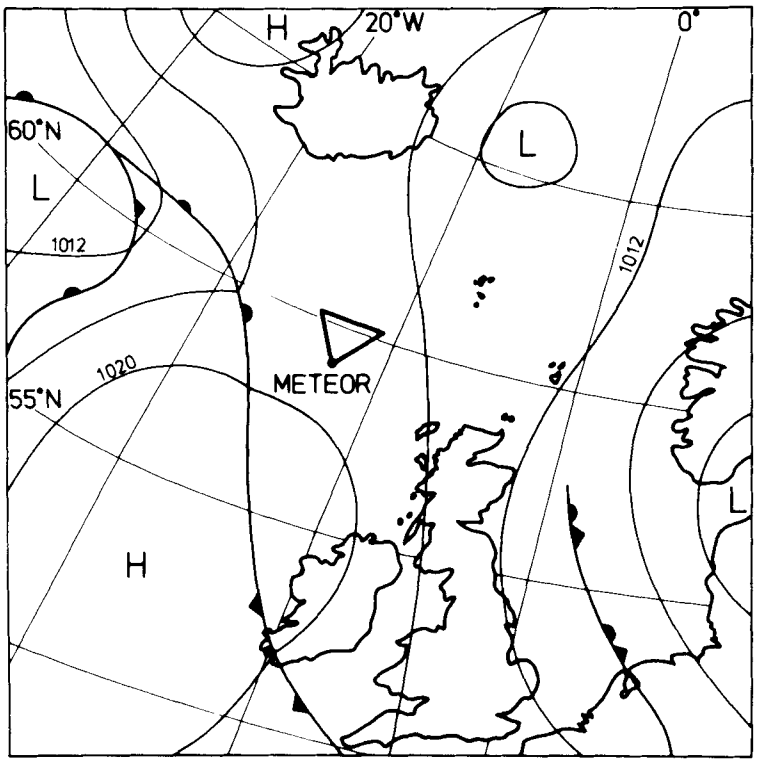

Figure 1. Geographical location of the JASIN experiment and surface synoptic situation at 1200 GMT on 1 September 1978. Meteorological measurements are made at the corners of the triangle (southern corner: *R.V. Meteor*).

2. Data sources and processing

As mentioned above, the data used in this study were obtained from radiosondes and a tethered balloon system at the *R.V. Meteor*. The radiosondes and their accuracy are described by Taylor *et al.* (1983). Between 0530 and 2030 GMT thirteen radiosondes were released at 1 to 2 hour intervals. Data at 5 mb intervals in the lowest 1500 m of the atmosphere are used in this study.

The tethered sonde system consisted of three sondes attached at about 750, 510 and 270 m to the tethering cable of the balloon, which was at about 900 m height. Additional measurements at 8 m above the sea surface were taken by a probe on a 5 m boom at the bow of the ship. At all four probes the dry and wet bulb temperatures (T, T_{wb}) were measured by ventilated thermistors installed in a downward pointing tube. This turned out to be an effective protection against the effects of cloud droplets on T. Pressure (p) was measured with a digiquartz and wind speed (U) with a cup anemometer. In addition, the following parameters were recorded at the tethered sondes: the three wind components (u, v, w) relative to the sonde were measured by hot film sensors; the three components of the earth's magnetic field (**H**) by magnetometers; and the three components of the acceleration vector (**a**) by accelerometers. Except for some occasionally

occurring isolated spikes, the hot films were not affected (e.g. caused to drift) by cloud droplets. A device measuring visible radiation from ten different angles, with aperture angles of 20 degrees, was installed in each package to detect the presence of cloud. Finally, for completeness, a platinum resistance thermometer should be mentioned, though this is not used in this paper. Further details on the instrumentation are listed in Table 1. Ship-related data, such as speed, heading, latitude and longitude, etc., were recorded at 0·5 Hz. A six-hour-long time series of the tethered sonde system data between 0925 and 1525 GMT is used in this study.

TABLE 1. BOOM AND TETHERED SONDE INSTRUMENTATION

Parameter	Sampling rate (Hz)	Resolution	Accuracy	Approximate sensor response (Hz)	Primary sensor
		Tethered sondes and booms			
T, T_{wb}	2	0·01 K	0·1 K	1	Thermistor
U	2	0·01 m s^{-1}	± 1% of mean	4*	Cup anemometer
p	10/2	0·025 mb	0·1 mb	10	Digiquartz**
		Tethered sondes			
T	10	0·003 K	0·1 K	10	Platinum resistor
u, v, w	10	0·005 m s^{-1}	$\bar{w} = 0$	10	3-D hot film
H	10	60 nT		10	3-D magnetometer
a	10	0·005 m s^{-2}		10	3-D accelerometer

* In a wind speed of 5 m s^{-1}.
** Quartz resonator changing resonance frequency with ambient pressure.

Location and orientation of the tethered sonde in space vary with time and this leads to erroneous wind measurements. The main noise signal is due to the ship's pitch and roll motions, which are transferred via the cable. Stretching and relaxing of the cable result in upward, downward, forward and backward motions as well as orientation variations of the sonde, with periods between 5 and 10 s. Balloon motions are also transfered to the packages. The orientation of the sonde in an earth-related coordinate system is determined from the magnetic field vector and an additional closure hypothesis of a constant value of the angular deviation of the sonde's y axis from the horizontal plane (the y axis is the more or less horizontal axis perpendicular to the long axis of the cylindrical body of the sonde which is pointing into the wind). It was intended to eliminate the effects of sonde motion on the measured wind in the spectral band of the ship's pitch and roll motions by integration of the acceleration data. However, it turned out that this could not be performed with sufficient accuracy, for reasons which are discussed by Fischer *et al.* (1987), so that the wind had to be determined in a different way. The measured wind vector is rotated in the earth-related coordinate system. Then, all three wind components are smoothed by a low-pass filter with a 12 s cut-off period. Due to the finite length of the balloon cable and the strong lift of the balloon, longer-period horizontal motions of the packages should be clearly below 1 m s^{-1} and vertical motions should be even smaller. However, since the natural vertical wind is also small, vertical motion of the sonde over periods longer than 12 s is corrected using the pressure measurements. The resulting corrected vertical wind is finally detrended with a running 5 min-average because variations on the order of 0·1 m s^{-1} for periods longer than 5 min cannot be interpreted as absolutely correct. Taken together, this results in a low-pass filtered horizontal wind and a band-pass filtered vertical wind in the period range between 12 s and 5 min corresponding to a range of horizontal wavelengths between 96 m and

2·4 km (assuming a mean wind speed of 8 m s^{-1}). In this spectral range the overwhelming part of the vertical transport takes place—at least at heights above 270 m (the level of the lowest sonde). Thompson *et al.* (1980) argue that at these heights the contribution from periods shorter than 12 s (96 m) to the sensible and latent heat flux is negligible and to the momentum flux is not more than 10%. For lower levels the omitted contributions would be larger, of course.

3. Thermodynamic and kinematic structure of the boundary layer

On 1 September 1978 a high pressure centre was situated west of Ireland leading to a west-north-westerly air flow with speeds of 7 to 8 m s^{-1} at 10 m in the JASIN area. In the course of the day a ridge moved over the area followed by an approaching warm front (Fig. 1) so that the wind decreased to about 6 m s^{-1} and backed to westerly. NOAA 5 satellite pictures in the visible and infrared channels show non-uniform low-level cloudiness with varying coverage over the experimental region.

Based on radiosonde ascents and cloud observations by eye at *Meteor* the following boundary layer structure is analysed (Fig. 2): a mixed layer, a transition layer, a cloud layer and an inversion layer. The cloud layer consisted of two separate layers during the period 0530 to 1400 GMT: a lower cumulus (Cu) layer with cumulus humilis, stratocumulus and cumulus fractus and an overlying thin stratocumulus (Sc) cloud layer. The cloud amount in the Cu layer mostly varied between 0 and 3 octas but even increased to 6 octas in a mesoscale Cu cloud field which passed over the station between 1045 and 1410 GMT. Afterwards, the Sc cloud deck also disappeared and for about 1·5 hours the boundary layer was free of cloud. The dissipation of the Sc and the sinking of the inversion base from 1050 to 700 m were presumably associated with the descending motion due to the high pressure ridge (Guymer *et al.* 1983). Later, at about 1600 GMT, low-level Cu clouds occurred again but without an overlying Sc layer. The lifting condensation level (LCL) calculated from the mean temperature and humidity in the mixed layer, is assumed as the base of the Cu clouds in Fig. 2. This estimate agrees with the radiometer measurements of the lowest two tethered sondes. The tops of the Cu clouds are not exactly known, but were generally below the Sc base. The Sc cloud base is obtained from the time of entry

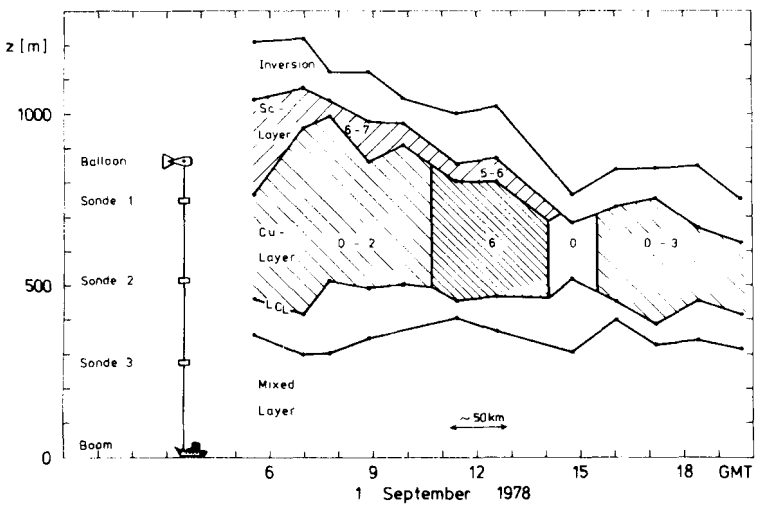

Figure 2. Boundary layer structure analysed from radiosonde ascents (dots). Figures in the cumulus and stratocumulus layer represent the cloud coverage in octas.

of the radiosondes into the Sc clouds observed by eye (by chance most radiosondes ascended between the lower Cu clouds).

The two cloud layers (Cu below Sc) can be analysed from each radiosonde ascent between 0535 and 1235 GMT. As the clearest example the 0745 GMT ascent is presented in Fig. 3. Besides the profiles of temperature, specific and relative humidity, the figure also illustrates the LCL for different starting levels and the energy $E(z, \mathrm{LCL})$ which a parcel at z needs to reach LCL. There are two steps in the LCL(z) curve around 500 m and 900 m, respectively. The lower step has been assumed as the Cu base, the upper one coincides with the observed Sc base. The Cu clouds have roots in the mixed layer (see also Fig. 10). The Sc roots appear to be in the upper part of the Cu layer. Direct coupling between Cu and Sc, in the sense that the Cu clouds extended into the Sc deck, was not visible. Parcels in the lower part of the Cu layer have their LCL also at the Sc base but presumably do not reach this level due to the relatively large energy needed (E about -4 J/kg). On the other hand the E values in the mixed layer indicate that Cu clouds can be generated with relatively small energies (E about -1 J/kg). The shape of the E curve, with a minimum around cloud layer base, is similar for all radiosonde ascents, although the minimum is less pronounced during the passage of the mesoscale Cu cloud field, when the air in the entire boundary layer is moister.

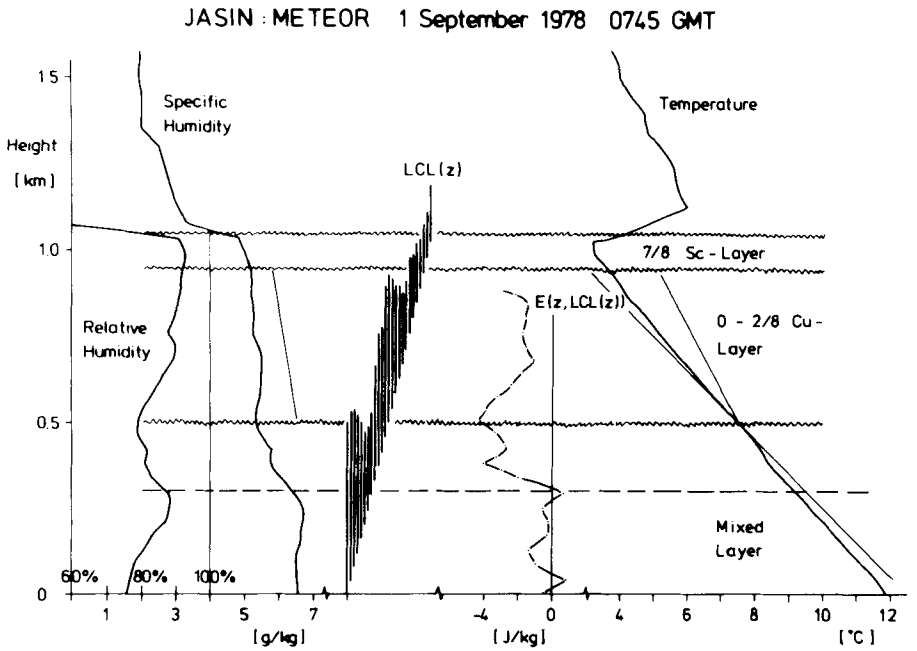

Figure 3. Profiles of temperature, relative and specific humidity, lifting condensation level, LCL, and energy $E(z, \mathrm{LCL}(z))$ required to reach LCL for radiosonde ascent at 0745 GMT. Thin straight lines near the temperature and specific humidity profiles indicate dry and moist adiabatic lapse rates.

Variations of potential temperature and specific humidity in the boundary layer connected with the above mentioned Cu cloud field are displayed in Fig. 4. The profiles represent 10 min averages based on boom and tethered sondes measurements. In the presence of Cu clouds the temperature in the mixed layer is up to 0·2 K lower and the moisture in the mixed layer and cloud layer is about 0·2 to 0·5 g/kg higher than in the preceding and following periods without these clouds. These variations imply lower LCL values and favour cloud development. At about 1420 GMT the sinking inversion reaches

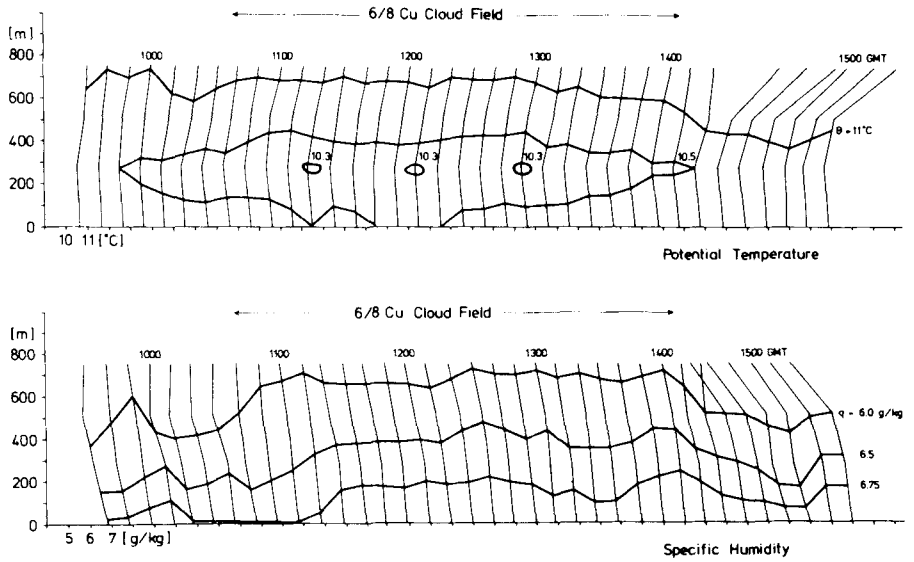

Figure 4. Mean vertical profiles (10 min averages) of potential temperature θ and specific humidity q determined from tethered sonde and boom measurements between 0925 and 1525 GMT (thin lines); thick lines represent isolines. Each graduation on the abscissa marks the 10 degC (5 g/kg) value of consecutive $\theta(q)$ profiles. The distance between two graduations also represents 1 degC (1 g/kg) difference in $\theta(q)$. The scales for the first (0925–0935 GMT) profile are given on the abscissae.

the level of the highest sonde (750 m) with warm and dry air, as can be seen from the last six profiles in Fig. 4.

There is indirect evidence that the mesoscale temperature and humidity variations in the boundary layer were caused primarily by advection. Other plausible physical mechanisms, for example a mesoscale variation of horizontal wind divergence, a variation of surface fluxes, or that the effect was caused by the convection itself, are not supported by the observations. A mesoscale horizontal wind convergence of about $-1{\cdot}5\times10^{-4}\,s^{-1}$ in the lowest 500 m in the case of a vanishing horizontal humidity gradient would be necessary to account for the observed 0·25 g/kg humidity increase within two hours. This corresponds to an upward vertical velocity of $0{\cdot}08\,m\,s^{-1}$ at 500 m and is an order of magnitude larger than any mesoscale vertical velocity analysed by Guymer *et al.* (1983) for this day. In addition, the sinking inversion (Fig. 2) implies large-scale subsidence rather than upward motion. If surface flux variations would have been the reason for the temperature and humidity changes in, for example, a 500 m-deep layer, then the sensible heat flux must have decreased by about $14\,W/m^2$ and the latent heat flux increased by about $50\,W/m^2$ for a period of about two hours. However, the observed surface heat and moisture fluxes and their variations at *Meteor* on this day were only $5 \pm 1{\cdot}5\,W/m^2$ and $50 \pm 8\,W/m^2$, respectively. The convergence of the turbulent moisture flux shown in Fig. 9 is on the order of the quoted $50\,W/m^2$ per 500 m depth, but the difference between the periods without and with clouds is much smaller. Likewise, an increase of the sensible heat flux by $14\,W/m^2$ and a decrease of the latent heat flux by $50\,W/m^2$ at 500 m were not observed between the periods with and without clouds (Fig. 9). Furthermore, convection would dry the lower levels and moisten the upper levels, but the moistening is observed within the whole boundary layer. Therefore we conclude that the mesoscale cooling and moistening were probably advectional effects and that the development of convection is favoured in this new environment.

Vertical profiles of wind speed and wind direction are shown in Fig. 5. The full curves represent averages over four radiosonde ascents (0953, 1125, 1235 and 1444 GMT) and the dots are averages over the period 0925 to 1525 GMT of the tethered sonde data. The two techniques differ by less than $0{\cdot}5\,m\,s^{-1}$ for wind speed and by less than 5° for wind direction. The boom wind speed at 8 m in the logarithmic layer is clearly smaller than the lowest radiosonde wind, at 40 m. Additional wind measurements at the ship's mast at 23 m give a $1{\cdot}2\,m\,s^{-1}$ higher wind speed than at the boom. Accordingly, the wind speed has a weak maximum at low levels, decreases with height in the boundary layer and increases above the inversion. The wind veers by nearly 30° between the mixed layer and the inversion. The largest veering together with an inflection point in the wind direction profile occurs in the Cu cloud layer. This particular shape of the profile, together with repeated visual observations of longitudinal cumulus cloud organization during the period of the Cu cloud field (noted in the tethered sonde logbook), brings us to the idea that dynamic instability (inflection point instability) may be involved in the occurrence of Cu clouds.

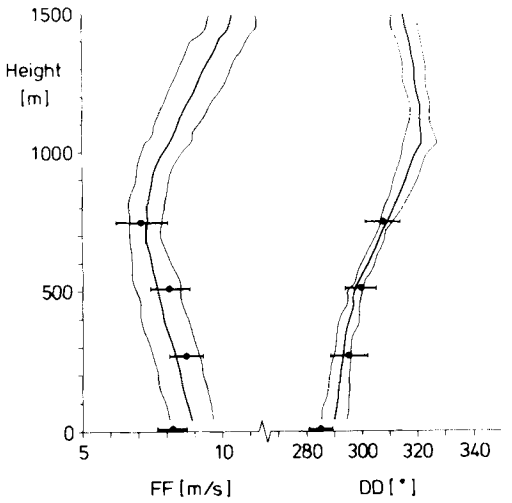

Figure 5. Mean values and standard deviations of wind speed FF and wind direction DD averaged over four radiosonde ascents (0953, 1125, 1235, 1444 GMT) and over the 6 h period of tethered sonde and boom measurements (full circles and horizontal bars).

This is supported by the chronological sequence of the four radiosonde wind profiles plotted in coordinates oriented parallel (u_s) and perpendicular (v_s) to the wind direction near the surface (Fig. 6). The 0953 GMT ascent before the passage of the Cu cloud field shows the largest v_s shear and an inflection point in the v_s profile close to the inversion. The profiles at 1125 and 1235 GMT measured during the passage of the cloud field show a clearly marked inflection point in the middle of the cloud layer. After the passage of the cloud field (1444 GMT) there is no significant inflection point in the boundary layer. These are hints that not only the thermodynamic but also the dynamic conditions for cloud generation are favourable during the passage of the cloud field. In Table 2 the generation rates of kinetic energy (within the spectral range from 100 m to 2500 m as mentioned in section 2) due to buoyancy ($(g/\bar{\theta})\overline{w'\theta_v'}$, where g is earth's gravity and θ, θ_v are potential and virtual potential temperature, respectively) and wind shear ($-\overline{w'v_s'}\,\partial v_s/\partial z$, $-\overline{w'u_s'}\,\partial \overline{u_s'}/\partial z$) at the two levels in the cloud layer are listed for the cases without and with clouds. Without clouds the total generation of kinetic energy in the cloud layer is small. With clouds it is 10 times larger and the shear generation contributes more than half to it. This shows that shear generation of kinetic energy (including cloud-

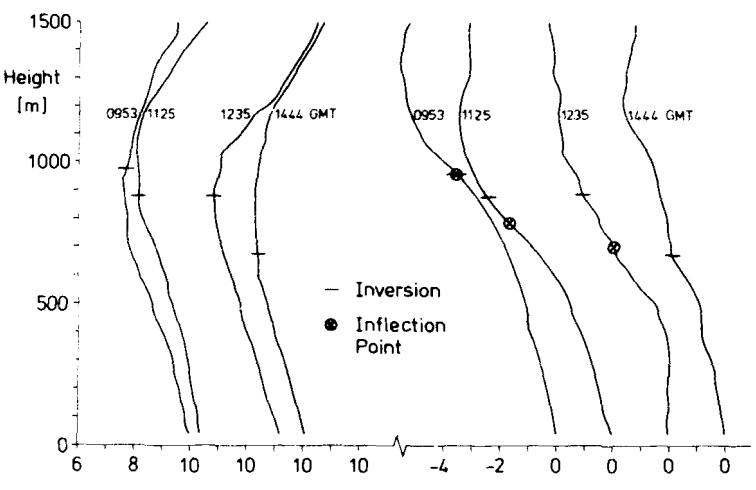

Figure 6. Profiles of wind components parallel (u_s) and perpendicular (v_s) to the wind near the sea surface from radiosonde ascents at 0953, 1125, 1235 and 1444 GMT.

TABLE 2. DYNAMIC AND THERMAL GENERATION OF KINETIC ENERGY AT 510 AND 750 m WITHOUT AND WITH Cu CLOUDS (UNITS $10^{-3}\,m^2\,s^{-3}$). THE GENERATION RATES ARE CALCULATED FROM THE VERTICAL GRADIENTS IN FIGURE 6 AND THE FLUXES IN FIGURE 9.

	Dynamic generation		Thermal generation	
Height	$-\overline{u_s' w'}\,\partial\bar{u}_s/\partial z$	$-\overline{v_s' w'}\,\partial\bar{v}_s/\partial z$	$(g/\bar{\theta})\,\overline{w'\theta_v'}$	
750 m	0·01	0·05	−0·01	Without clouds
510 m	0·02	0·04	0·00	
750 m	0·06	0·15	0·18	With clouds
510 m	0·01	0·12	0·05	

scale kinetic energy) is not negligible in this case and may be a sensitive trigger mechanism for cloud formation.

The reasons for the appearance and disappearance of the inflection point in the v_s profile are not known. It may simply be an advectional effect. Another possible physical mechanism could be an interaction between the mean flow and convection. By favourable large-scale conditions a shear zone with an inflection point is set up in the mean wind profile. If the wind shear is sufficiently large and its height is favourable (not too close to the top of the boundary layer), convection is generated dynamically (Brümmer and Latif 1985). However, convection acts to reduce the mean wind shear and consequently its kinetic energy supply ($\overline{w'v_s'}\,\partial\bar{v}_s/\partial z$), so that it weakens and finally decays. If favourable large-scale conditions, as at the beginning, still exist a wind shear zone with an inflection point may develop again. This idea, however, cannot be tested with our data. The $\overline{w'v_s'}$ flux measurements by the tethered sondes (Fig. 9) are not accurate enough to compare e.g. $\partial\bar{v}_s/\partial t$ between 1235 and 1444 GMT (Fig. 6) with the vertical divergence of the flux difference between the situation with and without clouds,

$$-\frac{\partial}{\partial z}\left[(\overline{w'v_s'})_{\text{with}} - (\overline{w'w_s'})_{\text{without}}\right].$$

This would require an absolute accuracy of the $\overline{w'v'_s}$ flux measurement better than $0{\cdot}01\,m^2\,s^{-2}$, which we do not have. Therefore, this idea has to remain speculative.

4. Heat and momentum transports without and with cumulus clouds

The above-mentioned Cu cloud field is analysed in more detail using the shortwave radiometer measurements from the tethered sondes (Fig. 7). A cloud passing underneath a sonde is indicated by a smaller signal (brighter) from the downward facing radiometer, a cloud above the sonde by a larger signal (darker) from the upward facing radiometer. If both radiometers show these signals simultaneously the sonde is inside cloud. The variations in the upward looking radiometer data due to Cu clouds are small because of other overlying clouds (Sc layer and also higher-level clouds). Concerning the vertical extent of the clouds, six different types can be distinguished within the cloud field: (1) clouds below 510 m; (2) between 510 and 750 m; (3) above 750 m; (4) from below 510 to below 750 m; (5) from below 510 to above 750 m; and (6) from below 750 to above 750 m. Clouds extending through the whole cloud layer, about 400 m deep (type 5), are most frequent and have a mean horizontal extent of about 450 m. Clouds of type 6 and 4, which occur in the upper or lower half of the cloud layer, are the next most frequent and on average about 290 and 380 m wide, respectively. Cloud types 1 to 3 are less frequent. The amount of type 3 Cu cloud is somewhat uncertain, because it is difficult to distinguish between them and overlying Sc clouds. The largest horizontal dimension of a single cloud is 850 m. The distance between individual clouds varies between 200 and 3500 m. From the downward facing radiometer of the highest package a coverage of 54% is estimated for the whole Cu cloud field.

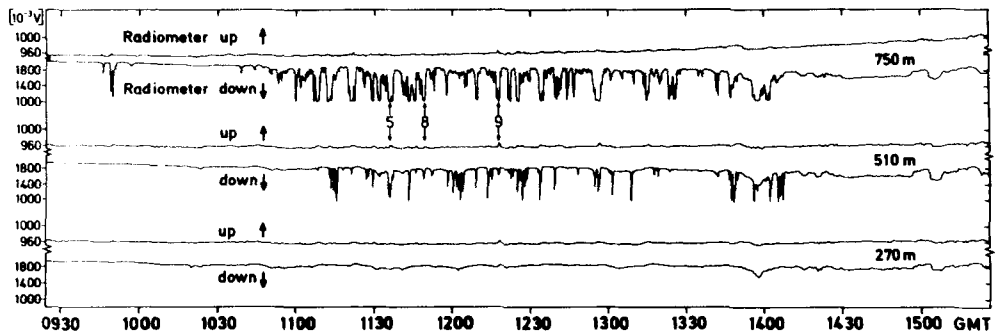

Figure 7. Time series of data from the upward and downward looking shortwave radiometers on the tethered sondes at 270, 510 and 750 m height. The locations of the three clouds presented in Figs. 10(a)–(c) are indicated by the numbers 5, 8 and 9.

For the computation of vertical transports, the time series of temperature, humidity and horizontal wind components are treated by the filter method used for the vertical wind component (see section 2). The transports of sensible and latent heat as well as u_s and v_s momentum averaged over 12 seconds are displayed in Figs. 8(a)–(d) for a period of six hours. The data from the downward facing radiometer at 750 m are repeated in the figures in order to facilitate a comparison between fluxes and clouds. The passage of the cloud field is clearly reflected in the time series for the levels 510 and 750 m: fluxes and their variations are small outside the cloud field and large excursions occur within it. Extreme values are always connected with individual clouds, but not every cloud is connected with extreme values. In the subcloud layer at 270 m these differences between the fluxes inside and outside the cloud field are not so obvious as in the cloud layer.

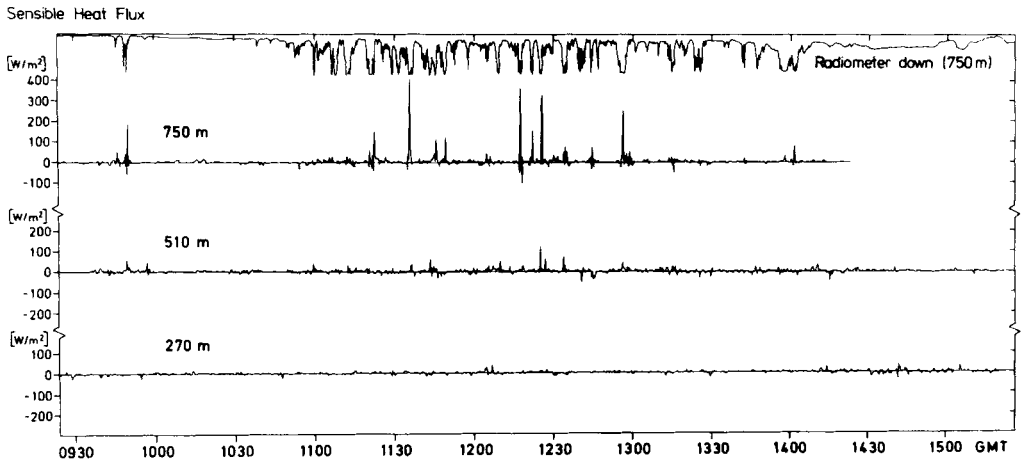

Figure 8(a). Time series of sensible heat transport at 270, 510 and 750 m averaged over 12 seconds after filtering the vertical wind and potential temperature data with a band-pass filter between 12 seconds and 5 minutes. The time series at the top of the figure represents the data from the downward looking radiometer at 750 m as already shown in Fig. 7.

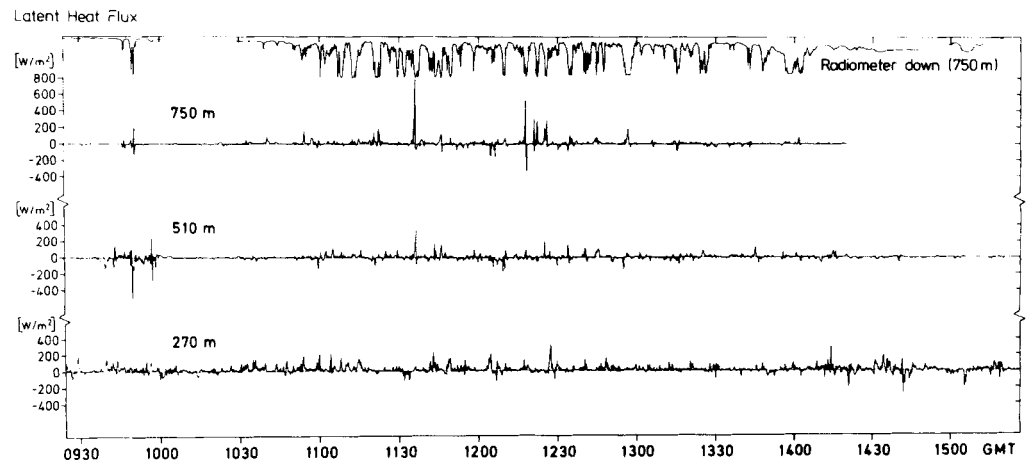

Figure 8(b). As Figure 8(a) but for latent heat.

Large fluxes at this level are not always related to overlying clouds but also occur in intermediate zones. Sensible heat flux excursions are predominantly positive with increasing amplitudes with height. This probably reflects the latent heat release in clouds at 750 m, and the fact that the sonde at 270 m is near the level of vanishing buoyancy generally located in the upper half of mixed layers heated from below. Latent heat flux variations are also predominantly positive and of similar amplitude at all levels. Momentum flux excursions have both signs, but for the v_s momentum flux, positive excursions dominate, especially at 270 m. Between 1200 and 1400 GMT the $v_s w$ time series at 270 m appears to show nearly periodic bursts of positive $v_s w$, the period being about 30 minutes. The interval between these bursts is similar to the periods of roll vortices found by LeMone (1973) for fixed point measurements. This may provide further evidence for the presence of longitudinal cloud organization within the mesoscale Cu cloud field.

Average transports for periods without and with cumulus clouds are presented in Fig. 9. For the case without clouds the time intervals 0925–0945, 1001–1045, 1410–1525 GMT (a total of 139 minutes) and for the case with clouds the intervals 0945–1001,

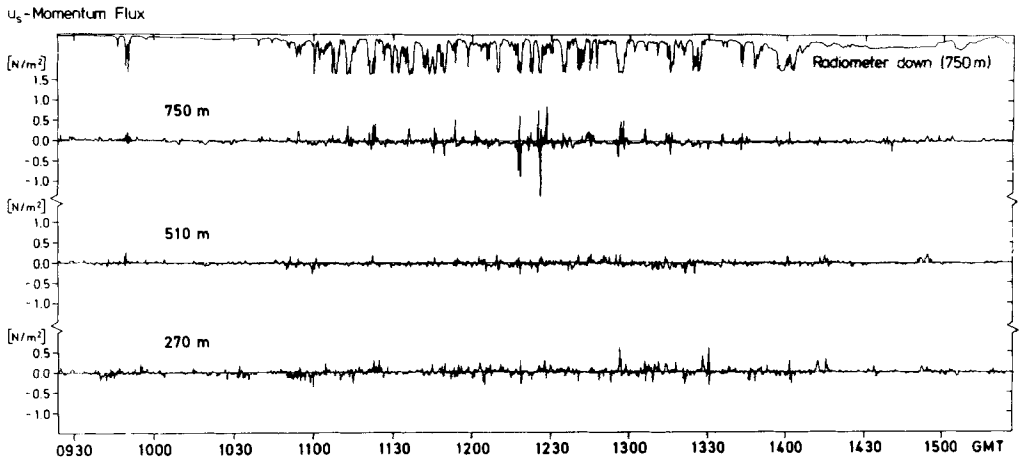

Figure 8(c). As Figure 8(a) but for u_s momentum (u_s is the horizontal wind component parallel to the mean wind direction of 285°).

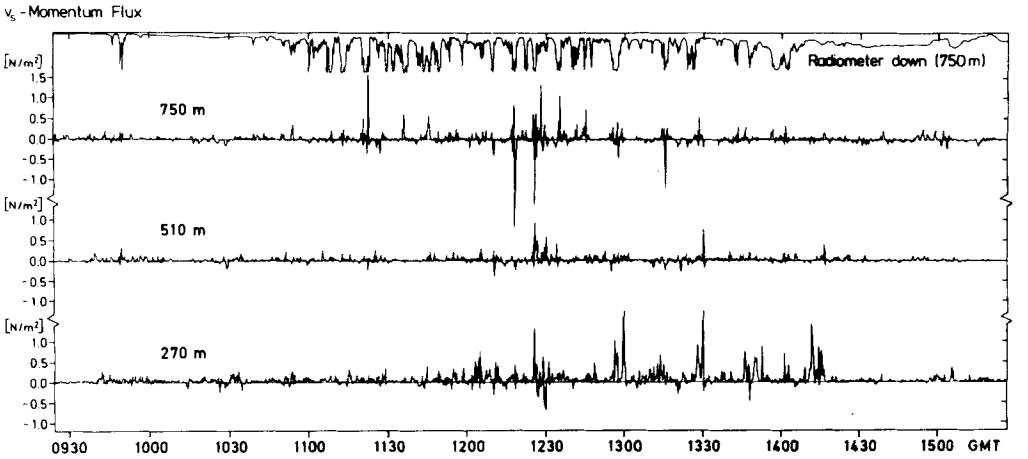

Figure 8(d). As Figure 8(a) but for v_s momentum (v_s is the horizontal wind component perpendicular to the mean wind direction of 285°).

1045–1410 GMT (221 minutes) are selected. Transports near the sea surface are calculated from the boom data of temperature, moisture and wind and from the bucket water temperature using the well-known bulk aerodynamic formulae with the same transfer coefficient of $1{\cdot}25\times10^{-3}$ for heat, moisture and momentum. The surface fluxes are nearly the same for both categories. The shape of the flux profiles is similar to other observations of slightly unstable boundary layers over sea which show decreasing sensible and latent heat fluxes, a decreasing u_s momentum flux and a negative v_s momentum flux in the subcloud layer. The differences between the fluxes (without/with clouds) are generally small and probably not even significant concerning the differences for the sensible heat flux in the subcloud layer, the latent heat flux at all levels, the u_s momentum flux at all levels and the v_s momentum flux in the cloud layer. Nevertheless, the signs of the differences for the θ, q and v_s fluxes are as would be expected, i.e. if the differences are assigned to the effect of the cloud field then it transports heat, moisture and v_s momentum upwards. The u_s momentum flux decreases rapidly with height and vanishes around 250 m. This is also observed by aircraft during JASIN (Nicholls *et al.* 1983), but is in

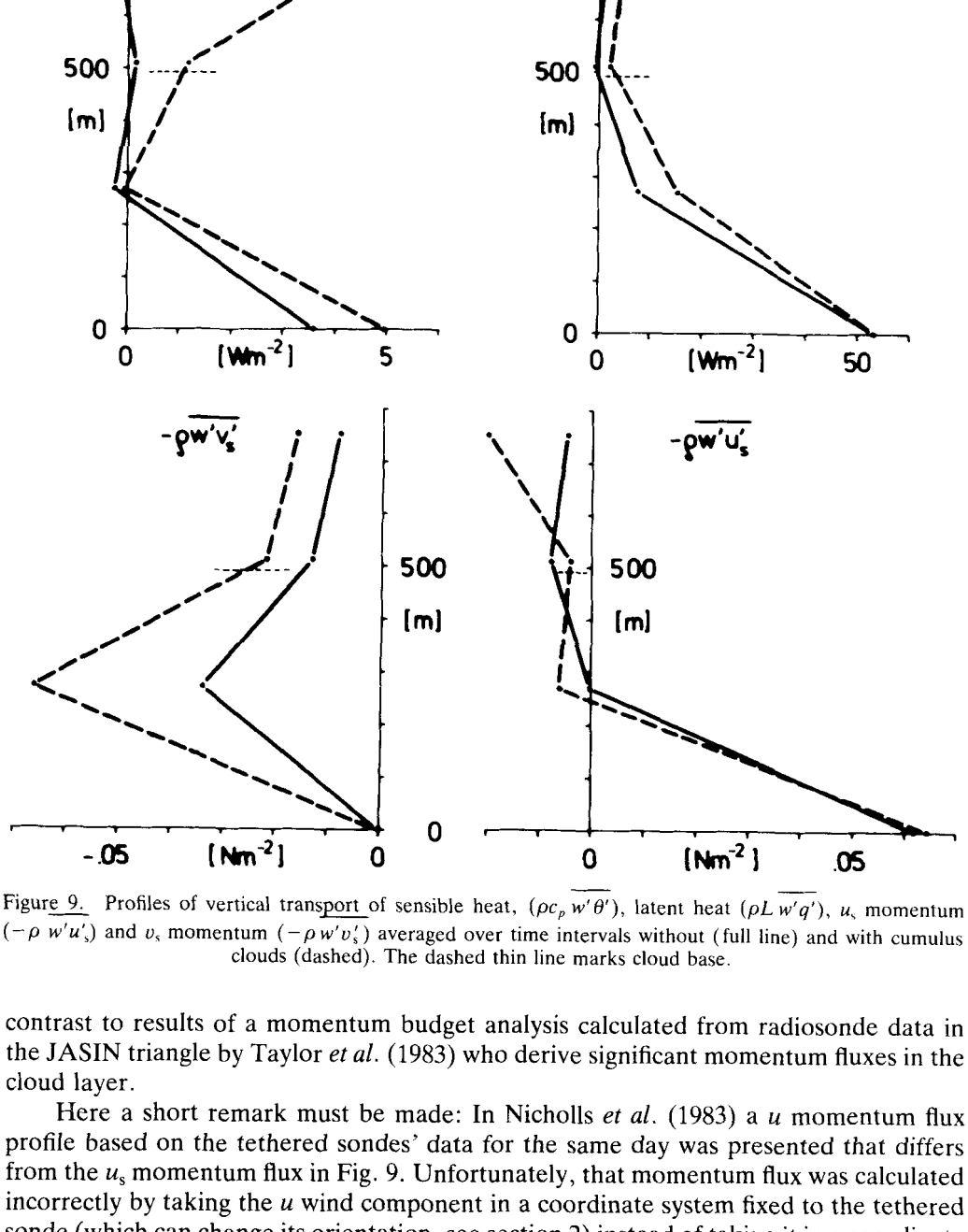

Figure 9. Profiles of vertical transport of sensible heat, ($\rho c_p \overline{w'\theta'}$), latent heat ($\rho L \overline{w'q'}$), u_s momentum ($-\rho \overline{w'u_s'}$) and v_s momentum ($-\rho \overline{w'v_s'}$) averaged over time intervals without (full line) and with cumulus clouds (dashed). The dashed thin line marks cloud base.

contrast to results of a momentum budget analysis calculated from radiosonde data in the JASIN triangle by Taylor *et al.* (1983) who derive significant momentum fluxes in the cloud layer.

Here a short remark must be made: In Nicholls *et al.* (1983) a u momentum flux profile based on the tethered sondes' data for the same day was presented that differs from the u_s momentum flux in Fig. 9. Unfortunately, that momentum flux was calculated incorrectly by taking the u wind component in a coordinate system fixed to the tethered sonde (which can change its orientation, see section 2) instead of taking it in a coordinate system fixed to the earth.

Although cloud cover within the cloud field is about 50%, transports by the field are small which is due to the fact that there are only a few large excursions in connection with a few active clouds. The bulk of the clouds seems to be inactive. In the following section three of the more active clouds are discussed in more detail.

5. Air flow and thermodynamic properties in and around clouds

Using the radiometer data, sixteen clouds were selected from the Cu cloud field in order to investigate the air flow and thermodynamic properties in and around them. The three wind components, potential temperature and specific humidity were averaged over successive 12 s intervals and over a period of several minutes centred around the considered cloud. The differences between the two averages represent the data set of this study. Since not all clouds can be shown here individually, only three (clouds 5, 8, 9) are selected for presentation in Figs. 10(a)–(c). The location of these clouds is marked in Fig. 7. They belong to those events connected with stronger flux signals in Figs. 8(a)–(d). Although some coarse similarities exist between the sixteen clouds, they are different in detail, of course, so that the three clouds presented here should be regarded as case studies.

The tethered sondes were not exactly aligned in the vertical direction. The horizontal displacement between the boom and the highest sonde was about 50 to 100 m. This corresponds to less than one time interval in Fig. 10, so that a time shift was not necessary.

The clouds are characterized by upward motion inside and downward motion near their boundaries. The strongest updraughts and downdraughts are found in the upper part of the clouds (750 m). At this level, the largest upward velocities (averaged over 12 seconds) are about 1·5 m s^{-1} and the largest downward velocities about 1·0 m s^{-1} (Fig. 10(c)). Updraught and downdraught velocities are of nearly comparable magnitude suggesting that the bulk of the updraught is compensated locally by a downdraught. The main part of the downdraught is found in the clear air near cloud edge, while only a small part is found on the cloudy side near cloud edge (as e.g. at 750 m on the upwind side of clouds 5 and 8).

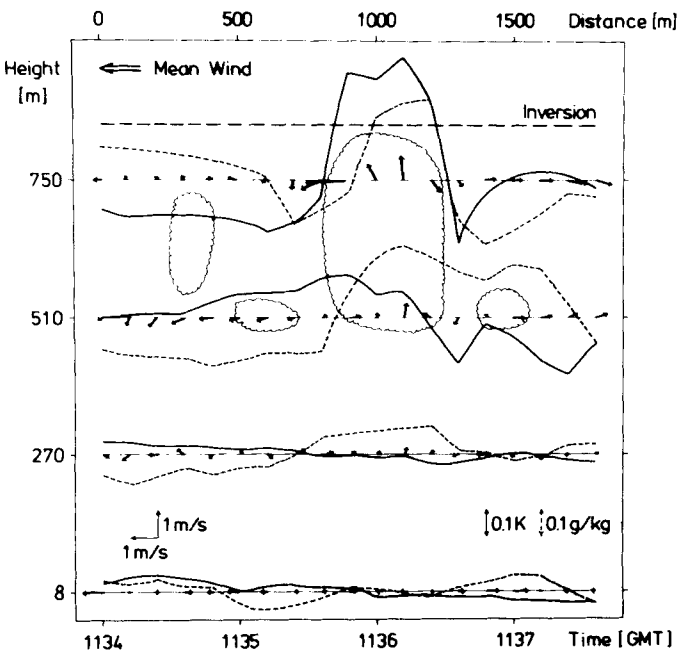

Figure 10(a). 12 s averages of potential temperature (full line), specific humidity (short dashes) and wind vectors (arrows) at 8, 270, 510 and 750 m in a vertical cross-section parallel to the mean wind direction for cloud 5 (see Figure 7). Cloud contours are marked by wavy lines and the inversion base is marked by long dashes.

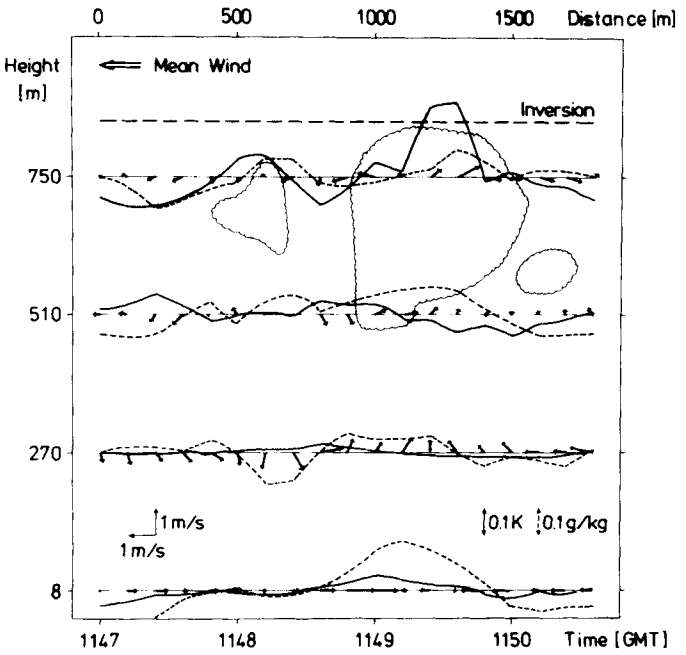

Figure 10(b). As Figure 10(a) but for cloud 8.

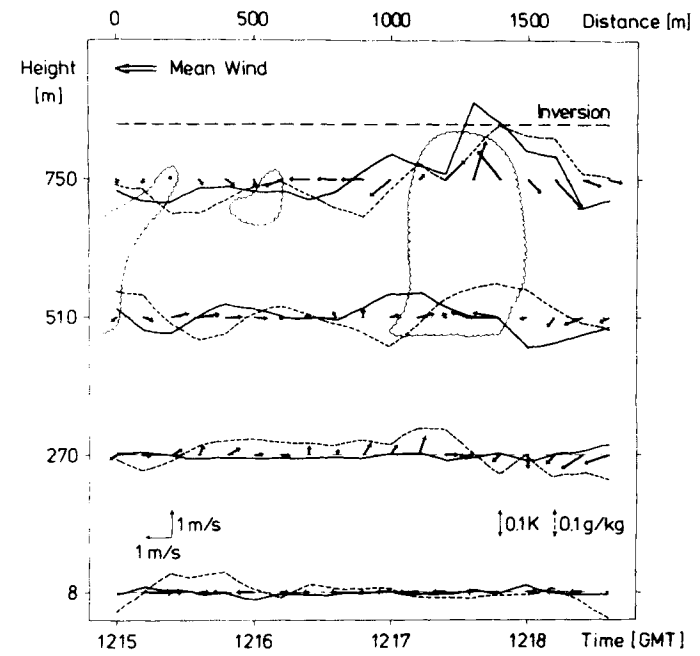

Figure 10(c). As Figure 10(a) but for cloud 9.

The updraught in the cloud is convergent (in the vertical plane parallel to the mean wind) near cloud base (510 m) in all three cases and is divergent at 750 m for clouds 5 and 8 and convergent for cloud 9. The downdraughts are directed from the cloud at 750 m and towards the cloud at 510 m, consistently for all three cases. Unfortunately, a vertical cross-section through clouds normal to the mean wind is not available so that conclusions about the total horizontal divergence of the draughts cannot be obtained. For the along-wind vertical plane the picture of a nearly symmetrical plume-like flow pattern in and around clouds is suggested. A more asymmetrical 'p-shaped' air flow pattern in the along-wind vertical plane in and around cumulus clouds of similar size was analysed by Kitchen and Caughey (1981) also from tethered balloon measurements. A different cloud-scale air flow in our case is not surprising because the mean wind profiles were different in the two cases: increasing wind speed with height in the cloud layer (Kitchen and Caughey) compared with a wind minimum in the cloud layer in our case (Fig. 5).

The central and probably least diluted part of the updraught in clouds is warm and moist. For the three clouds shown in Fig. 10 the largest temperature excess, compared with the 4-minute average value centred around the corresponding cloud, is between 0·25 and 0·4 K at 750 m and between 0·05 and 0·15 K at 510 m. The largest moisture excess amounts to between 0·1 and 0·25 g/kg at 750 m and also at 510 m. These deviations appear to be slightly smaller than for an undiluted moist adiabatic ascent. In that case the temperature and humidity excess can be estimated from the relationships

$$\Delta\theta = \left[\left(\frac{\partial\theta}{\partial z}\right)_{\text{m.ad}} - \left(\frac{\partial\theta}{\partial z}\right)_{\text{e}}\right](z - z_{\text{cb}}) + (\theta_{\text{cb}} - \theta_{\text{cb,e}}) \tag{1a}$$

$$\Delta q = \left[\left(\frac{\partial q}{\partial z}\right)_{\text{m.ad}} - \left(\frac{\partial q}{\partial z}\right)_{\text{e}}\right](z - z_{\text{cb}}) + (q_{\text{cb}} - q_{\text{cb,e}}). \tag{1b}$$

Assuming the moist adiabatic lapse rate is $(\partial\theta/\partial z)_{\text{m.ad}} \approx 3{\cdot}5$ to $4{\cdot}0\,\text{K}\,(1000\,\text{m})^{-1}$ and $(\partial q/\partial z)_{\text{m.ad}} \approx -1{\cdot}5\,\text{g kg}^{-1}(1000\,\text{m})^{-1}$, taking the environmental lapse rates from the two radiosonde profiles at 1126 and 1235 GMT as $(\partial\theta/\partial z)_{\text{e}} \approx 2{\cdot}0\,\text{K}\,(1000\,\text{m})^{-1}$ and $(\partial q/\partial z)_{\text{e}} \approx -2{\cdot}0\,\text{g kg}^{-1}(1000\,\text{m})^{-1}$, assuming at cloud base ($z_{\text{cb}} = 500\,\text{m}$) the same temperatures in the cloud and in the environment ($\theta_{\text{cb}} = \theta_{\text{cb,e}}$), but about 0·4 g/kg moister air in the cloud than in the environment, then from (1) at 750 m deviations of about 0·4 K for $\Delta\theta$ and about 0·5 g/kg for Δq are estimated. The difference from the observed values is only some tenths of 1 K and 1 g/kg and may be explained by lateral entrainment mixing between cloudy and environmental air.

The thermodynamic properties of downdraughts in the unsaturated air near the cloud edges are much more variable. All four possible sign combinations of temperature and moisture deviations are observed. Cold/dry downdraughts are present at 750 m on both sides of cloud 5 and on the downwind side of cloud 8, a warm/moist downdraught occurs at 750 m on the upwind side of cloud 9, cold/moist downdraughts are present at 510 m on the upwind sides of clouds 5 and 9, and a warm/dry downdraught is observed at 750 m on the downwind side of cloud 9. This shows that the downdraught is seldom an undiluted warm and dry compensating air flow in the clear air near cloud but is modified by other processes, for example by mixing with cloudy air and evaporation of cloud droplets. Evaporative mixing processes of cloudy and unsaturated air have been discussed by Paluch (1979) and Betts (1982). Paluch found observational evidence of downdraught formation due to cloud top entrainment in deep continental cumuli and Betts investigated theoretically the lateral entrainment mixing of cloudy and unsaturated air originating from different levels.

In our case, the observed $\Delta\theta, \Delta q$ downdraught properties may also be explained as the effect of an evaporative mixing process. We assume that the downdraught originates from the level z where environmental air is mixed with cloud air so that the mixture is still unsaturated and then descends dry adiabatically to the observation level z_*. For an accurate computation of the downdraught properties $\Delta\theta$, Δq at z_*, the environmental lapse rates $(\partial\theta/\partial z)_e$, $(\partial q/\partial z)_e$, the cloud properties, θ_c, q_c, l_c (liquid water content), at the mixing level z and the mass portions, x_e, x_c, involved in the mixing of environmental and cloudy air have to be known. Most of those parameters z, θ_c, q_c, l_c, x_e, x_c, were not measured. Only the environmental lapse rates are known from the radiosonde ascents. For the cloud air properties θ_c, q_c, l_c, the values from a moist adiabatic ascent through cloud base can be assumed as upper limits and the environmental values as approximate lower limits. Then, for various combinations of the parameters $\theta_c, q_c, l_c, z, x_e, x_c$, different $\Delta\theta$, Δq downdraught properties at the observational level z_* can be simulated. In this way it can be estimated which parameter combinations are responsible for the different $\Delta\theta$, Δq deviations of downdraughts. The following estimates are then obtained. (1) A cold/dry downdraught is possible for mixing levels between about 50 and 100 m above z_* (= 750 m) and if the cloud air involved in the mixing process has nearly the same θ— and q—values as the environment. Such cloud properties are probably present near cloud edge. (2) A cold/moist downdraught can be generated by mixing at z_* or not too far above z_* (less than about 40 m). (3) A warm/moist combination results if the cloud air involved in the mixing has clearly larger θ_c, q_c values than the environment, i.e. if air from the more central undiluted parts of the cloud is involved. And finally (4) warm/dry downdraughts are obtained by no or little evaporational mixing.

Supposing that the proposed mixing process was indeed responsible for the observed downward properties, then these simple estimates show how sensitively the downdraught properties depend on the mixing level, z, magnitude of mixing, x_e, x_c, and cloud properties, θ_c, q_c and l_c in a given environment. Radiative cooling may in addition be involved in the downdraught formation. However, in unsaturated air this process will only change θ, but not q. Furthermore, there may be an effect of the overlying thin Sc layer on the Cu clouds and on the properties of the downdraughts near clouds. However, our data are not sufficient to analyse this effect.

In the mixed layer (270 m) updraughts are predominantly moist and have only small temperature deviations, while downdraughts are predominantly dry and warm. This is in rough agreement with the picture of dry adiabatic motions in a layer with a small positive mean temperature lapse rate and a negative mean moisture lapse (Figs. 3 and 4).

6. Concluding remarks

The boundary layer described in this paper was not only observed on many days during the JASIN experiment (Taylor *et al.* 1983) but is also a frequent phenomenon in middle latitudes during situations with small surface heat fluxes. Stimulated by the case study presented, the intermittent character of the low-level cumulus clouds and the considerable dynamic contribution to cloud generation brought up the idea of an interaction between large-scale processes generating an inflection point in the mean wind profile and dynamically forced convection. The principles of such an interaction could be described, for example, by the following equations:

$$\Delta\dot{v} = c_1(\Delta v_L - \Delta v) \qquad \text{for} \quad \Delta v < \Delta v_c \qquad (2a)$$

$$\Delta\dot{v} = c_1(\Delta v_L - \Delta v) + c_2 \int_{\tau = t(\Delta v_c)}^{\tau = t} (\Delta v_c - \Delta v)\, d\tau \qquad \text{for} \quad \Delta v \geqslant \Delta v_c. \qquad (2b)$$

The velocity difference Δv between representative wind speeds above and below the inflection point is assumed as the relevant parameter for this problem. The local time variation of Δv is caused by a large-scale process (first term on the right of (2)) and the convective process (second term on the right of (2b)). It is assumed that the large-scale process depends on the deviation of Δv from a stationary final difference Δv_L which would be attained if the large-scale process acted alone. The convective process depends on the deviation of Δv from the wind difference Δv_c at which the convection is 'switched on' and on the time period over which the convective process is already working. The first process is always acting, the second only if Δv is larger than Δv_c. The coefficients c_1 and c_2 are a measure of the time scales of both processes. These coefficients, together with the values of Δv_L and Δv_c, determine the period of this interaction. In order to test Eqs. (2) quantitatively, our observations are not sufficient, unfortunately. However, the necessary parameters could, e.g., also be determined from a numerical convection model able to simulate inflection point instability.

The mean transports of heat and momentum by the field of low-level cumulus clouds are small. In the areas between clouds there are practically no transports. However, in connection with active clouds there are large transports up to several $100\,\mathrm{Wm^{-2}}$ and up to $1\,\mathrm{Nm^{-2}}$. These occur locally and not over the whole cloud area and can change (e.g. momentum flux) sign within the same cloud. The average transport is then a small residual of a few large excursions.

The air flow in and around active clouds is characterized by updraughts inside the clouds and downdraughts near the cloud boundaries. The central part of the updraughts is warm and moist, but the temperature and moisture deviations are slightly smaller than those for an undiluted moist adiabatic ascent. Downdraughts in the unsaturated air near cloud edge can have all possible sign combinations of temperature and moisture deviations. These may be explained as the effect of lateral mixing between cloudy and environmental air followed by descent of the mixture.

ACKNOWLEDGMENTS

Thanks are due to Drs M. Dunckel and J. Bösenberg from the Max Planck Institut für Meteorologie in Hamburg, who developed the tethered sondes and the data recording system. Dr G. Olbrück from the Seewetteramt Hamburg kindly prepared the VIZ radiosonde data.

REFERENCES

Albrecht, B. A., Betts, A. K., Schubert, W. H. and Cox, S. K. 1979 A model of the thermodynamic structure of the trade-wind boundary layer: Part I. Theoretical formulation and sensitivity tests. *J. Atmos. Sci.*, **36**, 73–89

Augstein, E. and Wendel, M. 1980 Modelling of the time-dependent atmospheric trade-wind boundary layer with non-precipitating cumulus clouds. *Contrib. Atmos. Phys.*, **53**, 509–538

Augstein, E., Schmidt, H. and Ostapoff, F. 1974 The vertical structure of the atmospheric planetary boundary layer in undisturbed trade winds over the Atlantic ocean. *Boundary-Layer Meteorol.* **6**, 129–150

Ball, F. K. 1960 Control of inversion height by surface heating. *Q. J. R. Meteorol. Soc.*, **86**, 483–494

Betts, A. K. 1982 Saturation point analysis of moist convective overturning. *J. Atmos. Sci.*, **39**, 1484–1505

Brümmer, B. and Latif, M 1985 Some studies on inflection point instability. *Contrib. Atmos. Phys.*, **58**, 117–126

Deardorff, J. W. 1974 Three-dimensional numerical study of the height and mean structure of a heated planetary boundary layer. *Boundary-Layer Meteorol.*, **7,** 81–106

Emmitt, G. D. 1978 Tropical cumulus interaction with and modification of the subcloud region. *J. Atmos. Sci.*, **35,** 1485–1502

Fischer, T., Wendel, M. and Brümmer, B. 1987 *Ein Fesselsondensystem zur Turbulenzmessung.* Hamburger Geophysikalische Einzelschriften

Guymer, T., Businger, J., Katsaros, K., Shaw, W., Taylor, P. K., Large, W. and Payne, R. 1983 Transfer processes at the air–sea interface. *Philos. Trans. R. Soc. London*, **A308,** 253–272

Kitchen, M. and Caughey, S. J. 1981 Tethered balloon observations of the structure of small cumulus clouds. *Q. J. R. Meteorol. Soc.*, **107,** 853–874

LeMone, M. A. 1973 The structure and dynamics of horizontal roll vortices in the planetary boundary layer. *J. Atmos. Sci.*, **30,** 1077–1091

Lenschow, D. H. 1970 Airplane measurements of planetary boundary layer structure. *J. Appl. Meteorol.*, **9,** 874–884

Lilly, D. K. 1968 Models of cloud-topped mixed layers under a strong inversion. *Q. J. R. Meteorol. Soc.*, **94,** 292–309

Nicholls, S. and LeMone, M. A. 1980 The fair weather boundary layer in GATE: The relationship of subcloud fluxes and structure to the distribution and enhancement of cumulus cloud. *J. Atmos. Sci.*, **37,** 2051–2067

Nicholls, S., Brümmer, B., Fiedler, F., Grant, A., Hauf, T., Jenkins, G., Readings, C. and Shaw, W. 1983 The structure of the turbulent atmospheric boundary layer. *Philos. Trans. R. Soc. London*, **A308,** 291–307

Paluch, I. R. 1979 The entrainment mechanism in Colorado cumuli. *J. Atmos. Sci.*, **36,** 2467–2478

Pennell, W. T. and LeMone, M. A. 1974 An experimental study of turbulent structure in the fair weather trade wind boundary layer. *ibid.*, **31,** 1308–1323

Pollard, R. T., Guymer, T. H. and Taylor, P. K. 1983 Summary of the JASIN 1978 field experiment. *Philos. Trans. R. Soc. London*, **A308,** 221–230

Sommeria, G. 1976 Three-dimensional simulation of turbulent processes in the undisturbed trade wind boundary layer. *J. Atmos. Sci.*, **33,** 216–241

Taylor, P. K., Grant, A. L. M., Günther, H. and Olbrück, G. 1983 Mass, momentum, sensible and latent heat budgets for the lower atmosphere. *Philos. Trans. R. Soc. London*, **A308,** 275–290

Tennekes, H. 1973 A model for the dynamics of the inversion above a convective boundary layer. *J. Atmos. Sci.*, **30,** 558–567

Thompson, N., Webber, K. L. and Norris, B. P. 1980 Eddy fluxes and spectra in the GATE sub-cloud layer. *Q. J. R. Meteorol. Soc.*, **106,** 277–292

Warner, J. and Telford, J. W. 1967 Convection below cloud base. *J. Atmos. Sci.*, **24,** 374–382